Influence of iron corrosion on nuclear glass alteration processes: nanoscale investigations of the iron-bearing phases

Charly Carrière, Delphine D. Neff, Eddy Foy, Christelle Martin, Yannick Linard, Nicolas Michau, James J Dynes, Philippe Dillmann

CORROSION ENGINEERING, SCIENCE AND TECHNOLOGY, 2017
VOL. 52, NO. S1, 166–172
https://doi.org/10.1080/1478422X.2017.1306962

The Institute of Materials, Minerals and Mining
Taylor & Francis
Taylor & Francis Group

Influence of iron corrosion on nuclear glass alteration processes: nanoscale investigations of the iron-bearing phases

Charly Carriere [a,b], Delphine Neff[a], Eddy Foy [a], Christelle Martin[b], Yannick Linard[b], Nicolas Michau [b], James Dynes[c] and Philippe Dillmann[a]

[a]LAPA-IRAMAT, NIMBE, CEA, CNRS, Université Paris-Saclay, CEA Saclay, Gif-Sur-Yvette Cedex, France; [b]Andra, Recherche et Développement, Châtenay-Malabry, France; [c]Canadian Light Source, Saskatoon, Canada

ABSTRACT

A carbon steel container including nuclear glass has been altered for 2 years in Andra's Underground Research Laboratory to simulate the behaviour of waste package. *Post-mortem* analyses at different scales (macro–micro–nano) have been performed to identify neoformed phases on iron corrosion products (ICP) and in the glass alteration layer (GAL). It has been shown at nanometric scale that important quantities of iron and silicon were found in the GAL and in the ICP respectively. Using a comparative approach with phyllosilicate references, STXM, at Si-K edge, suggests presence of trioctahedral species in the GAL and in ICP. Relevant fits of the STXM spectra are obtained with a Fe-rich chlorite for the nanostructured GAL, which could be formed according to chloritisation mechanism.

ARTICLE HISTORY
Received 4 November 2016
Accepted 2 March 2017

KEYWORDS
Nuclear glass; iron corrosion products; phyllosilicate; STXM; Si-K edge; chlorite; glass alteration layer

This paper is part of a supplement on the 6th International Workshop on Long-Term Prediction of Corrosion Damage in Nuclear Waste Systems.

Introduction

In the context of nuclear waste management, several strategies propose to confine high level radioactive waste (HLW) in a deep geological disposal. Andra (French National Radioactive Waste Management Agency) suggests a multi barrier system including the glass canister, a carbon steel overpack and a low permeability clay host rock to prevent borosilicate glass alteration and limit the release of radionuclides [1]. Although borosilicate glass is known for its high performance against water alteration [2], its lifetime must exceed thousands of years to immobilise HLW for safety reasons. Thus prediction on alteration of containment barriers of HLW is based on representative experiments at different timescales coupled with predictive modelling for the long term.

After burial of HLW and complete resaturation of the host rock, water will arrive to the near field, corrode the carbon steel overpack and induce glass hydrolysis. The near field is defined by Andra as 'part of a geological disposal facility for radioactive waste, including the host rock in the immediate environment. The near field is usually the seat of thermal, hydraulic, mechanical and chemical disturbances induced by the presence of nuclear waste'. Alteration of these two materials, the nuclear glass and the carbon steel overpack, have been studied separately for decades and more recently several studies have shown that the combined impairment of iron and glass can lead to a more intense alteration of the glass [3]. Indeed precipitation of neoformed phases such as iron-silicates, caused by the presence of silicon and iron ions in the solution, can modify and shift the physicochemical equilibrium of the solution. In return, the drop in glass alteration rate can be delayed [4]. That is why the iron-silicate species have to be identified and characterised to add important data for the glass–iron alteration model.

The aim of the study is to investigate, at different scales (micrometer and nanometer scale) with several analytical techniques, the alteration state of a system which simulate at a centimeter scale an inactive nuclear glass canister confined in a carbon steel overpack surrounded by claystone. The system has been altered in the Andra's Underground Research Laboratory (URL) at Bure (Meuse/Haute-Marne, France) for 2 years [5]. On the one hand, physicochemical analyses are performed on the altered glass, in the Glass Alteration layer (GAL), and in the Iron Corrosion Products (ICP) to describe the different alteration products and assess the preferential locations of iron-silicates precipitation. On the second hand, a comparative approach is led between iron-silicates found in the sample and phyllosilicate references in order to better understand the alteration of nuclear glass under geological disposal conditions.

Materials and methods

The studied system simulates a nuclear glass canister, consisting of a carbon steel (P275NL1, composition in Table 1) overpack (height 2 cm, diameter 2 cm) containing crushed inactive nuclear glass powder (SON68, composition Table 1), surrounded by claystone (Callovo-Oxfordian) (Figure 1). The particle size of the nuclear glass was between 0.63 and 1 mm, after being crushed, washed to remove impurity and sifted. The container had 10 small holes (diameter 1 mm) to allow water (composition in Table 2) to come in contact with the glass and the inside of the canister. The canister was then placed in a claystone piece, at 50°C under anoxic conditions in an interval of a 7 m-long vertical descending borehole drilled in a gallery at a depth of -490 m in Andra's

CONTACT Charly Carriere charly.carriere@cea.fr LAPA-IRAMAT, NIMBE, CEA, CNRS, Université Paris-Saclay, CEA Saclay 91191, Gif-Sur-Yvette Cedex, France

Table 1. SON68 glasses composition (TC42c) in weight per cent (a) and carbon steel P275 NL1 (b).

Oxides	SON68	Oxides	SON68
(a)			
SiO_2	45.82	Ce_2O_3	0.93
B_2O_3	14.02	La_2O_3	0.90
Na_2O	9.86	NiO	0.74
Al_2O_3	4.91	MnO_2	0.72
CaO	4.04	BaO	0.60
Fe_2O_3	2.91	Cr_2O_3	0.51
ZrO_2	2.65	Pr_2O_3	0.44
ZnO	2.50	SrO	0.33
Li_2O	1.98	P_2O_5	0.28
MoO_3	1.7	TeO_2	0.23
Nd_2O_3	1.59	Y_2O_3	0.20
Cs_2O	1.42	Other	0.08

(b)	
C	Max 0.16
Si	Max 0.4
Mn	0.8–1.5
Ni	Max 0.5
P	Max 0.025
S	Max 0.015
Cr	Max 0.3
Mo	Max 0.08
V	Max 0.05
N	Max 0.012
Nb	Max 0.05
Ti	Max 0.03
Al	Max 0.02
Cu	Max 0.3
Nb + Ti + V	<0.05
Fe	Rest

Table 2. Theoretical chemical composition of COx groundwater at 50°C [6].

Element	Concentration (mg L^{-1})
Na	966
K	39
Ca	397
Mg	100
Sr	18
Si	10
Cl	1453
SO_4	1345
HCO_3	232
pH (50°C)	6.86
Eh (50°C)	−140 mV/SHE

Underground Research Laboratory (URL) at Bure (Meuse/Haute-Marne, France). After 2 years, the system removed from the borehole and frozen and lyophilised to eliminate water. The canister was then embedded in resin, cut and polished to 1 µm roughness under a N_2 atmosphere in a glove box to limit oxidation.

Sample cross section (Figure 1) with nuclear glass, iron and claystone is observed and characterised first at microscopic scale. Observations were carried out at 15 keV with an energy-dispersive X-ray (EDX) system coupled to a field emission gun – scanning electron microscope (Jeol JSM-7001F). Micro-Raman spectroscopy (Invia Reflex® spectrometer) was performed by point analyses on regions of interest (ROI) with an excitation wavelength of 532 nm.

To investigate the iron–glass system alteration at the nanometer scale, synchrotron-based scanning transmission X-ray microscopy (STXM) analysis was used at the Fe-L- and Si-K-edges, on the 10ID-1 beam-line at the Canadian Light Source (CLS, Canada). Ultra-thin sections of 100 and 1 µm of the embedded sample were cut for examination at the Fe-L- and Si-K-edges, respectively, of the embedded sample were cut using a focused ion beam (FIB) (Helios Nanolab 650 equipped with electron and Ga ion beams). STXM, at Fe-L edge, is sensitive to the valence of iron containing phases (e.g. iron corrosion products, iron-silicates) and Si-K edge study provide information on the chemical environment of silicon contained in glass (pristine and altered) and iron-silicates. STXM data processing has already been described by many authors [7,8,3]. Three phyllosilicate references were chosen (Table 3) for the comparative approach because they represent the main end-members of Fe-bearing clay minerals. Greenalite (serpentine group, 1:1 clay), a nontronite (smectite group, 2:1 clay) and a chamosite (chlorite group, 2:1:1 clay) have previously been characterised by µRaman and µXDR to verify the nature and purity.

Results

Alteration facies at micrometer scale

SEM photograph presented on Figure 2 shows part of glass in the iron canister. The thicknesses of the GAL were about 1 ± 0.1 µm, regardless of the distance between the iron canister (i.e. iron source) and the glass powder. A specific zone was investigated, near the internal surface of the container, where both the iron and glass alteration products could be identified (Figure 3). The elemental composition of the pristine glass (PG), the GAL and ICP was analysed by EDX (Figure 3). The GAL is easily observable from the pristine glass due to a decrease in the glass network modifiers such as sodium and calcium due to glass hydration. Also the GAL was depleted in network formers (Zr, Al) due to glass hydrolysis [10]. Difference in contrast on the SEM image between PG and GAL could be used to locate the PG/GAL interface. Lastly, the GAL was enriched with iron and magnesium compared to PG. Considering the corrosion of the container, ICP was observable on elementary maps thanks to the presence of oxygen (Figure 3). ICP contained also around 20%wt of silicon, and traces of Na, Mg, Al and Ca (Table 4).

µRaman spectroscopy was used to characterise iron species in the ICP along the container and in the GAL. It

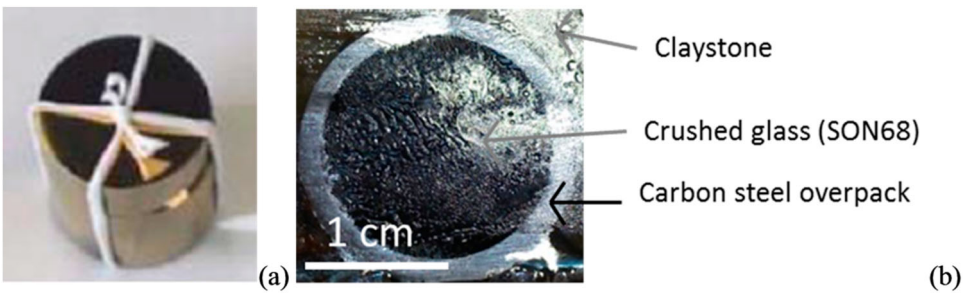

Figure 1. (a) Photograph of the canister (height 2 cm, diameter 2 cm), (b) cross section after being embedded in epoxy resin.

Table 3. Phyllosilicate references used for the comparative approach.

Mineral	Family	Formula (theoretical or experimental)
Greenalite	Serpentine – trioctahedral	$Fe^{II}_{2-3}Si_2O_5(OH)_4$
Nontronite (Garfield)	Smectite – dioctahedral	$Na_{0,4}Fe^{III}_2(Si, Al)_4O_{10}(OH)_2$ [9]
Chamosite	Chlorite – tri, trioctahedral	$(Fe^{II}, Mg)_5Al(AlSi_3)O_{10}(OH)_8$

was not possible to obtain Raman spectra from the GAL, even though the high Fe amount observed at this location by EDX suggest the presence of the precipitated Fe-SI species. On the contrary, Raman spectra from the ICP identified goethite (α-FeOOH) and a poor crystallised phase ferrihydrite ($FeOOH.nH_2O$) [11] (Figure 4). Goethite is characterised with Raman bands position at 299, 385, 548 and 681 cm^{-1} and a strong peak at about 700 cm^{-1} define ferrihydrite [12].

Iron-silicate investigation at the nanometer scale

A thin foil was cut with focused ion beam in order to investigate both ICP and GAL (Figure 5).

Image difference maps at the Si-K (Figure 6(a)) and Fe-L edges (Figure 6(b)) were obtained on the whole FIB foil to map the silicon and iron in the ICP and GAL. Two images at two energies were chosen, one at the edge (1846 eV for

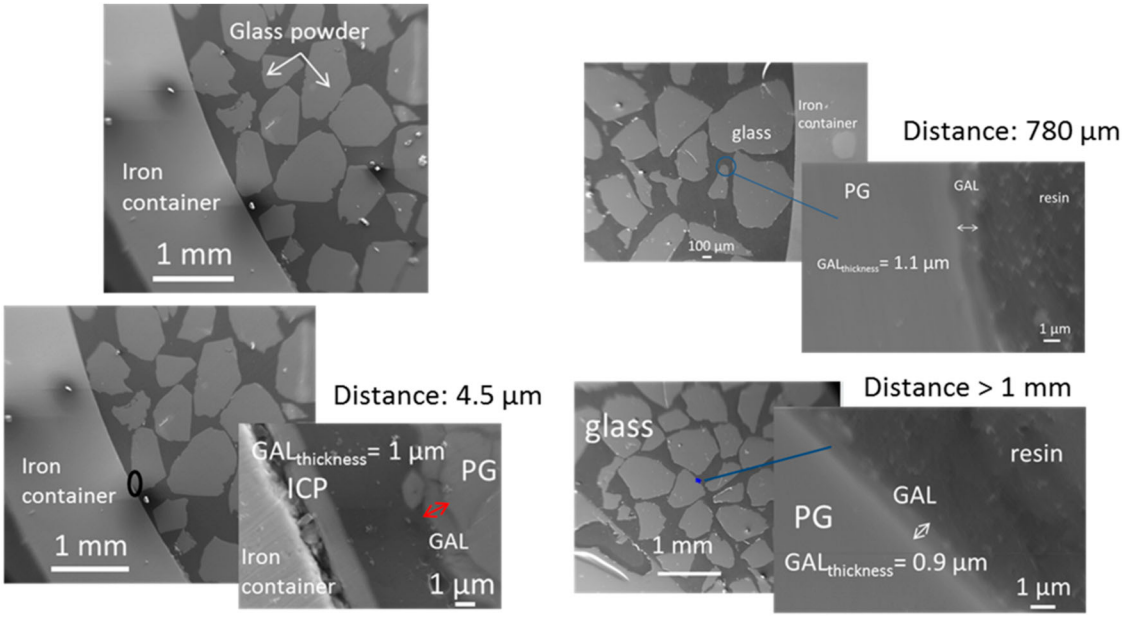

Figure 2. FEG-SEM of the iron container with nuclear glass powder inside and thicknesses of glass alteration layer (GAL) measured at different glass–iron distances. PG means pristine glass and ICP iron corrosion products.

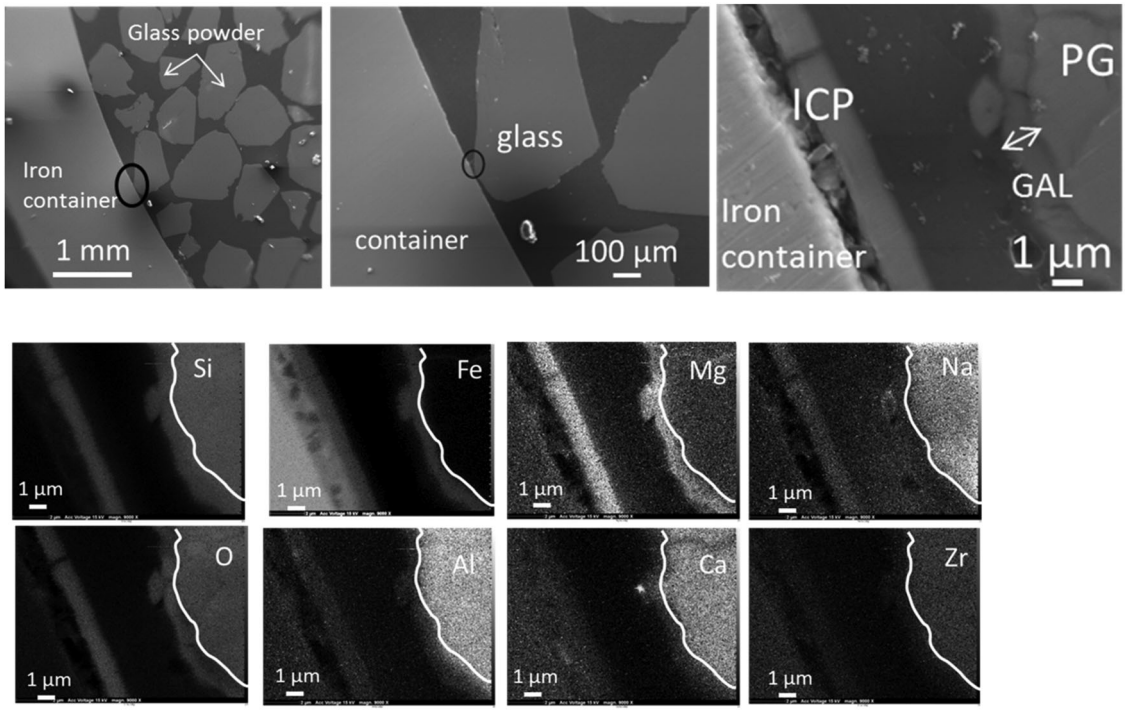

Figure 3. SEM and EDX elementary mappings on a zone with ICP and GAL. The white line separates PG and GAL.

Table 4. EDX chemical composition analysis (wt-%) of the GAL, PG and ICP.

	PG	GAL	ICP
Si	28.8	28	21.4
Fe	1.9	32.9	44.7
Mg	Detected	2	2.4
Na	2.1	Detected	Detected
O	35.5	32.8	28
Al	3.9	1	Detected
Ca	3.8	0.9	Detected
Zr	3.1	Detected	Undetected
Others (Zn, Mo, Cs, Ba, La, Ce, Nd)	20	/	/
SUM	99.3	98.2	98.1

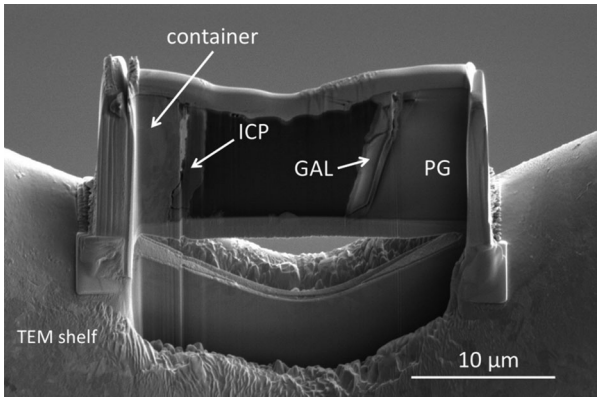

Figure 5. FIB section of the sample cut with FIB. Iron corrosion products of the container, glass alteration layer and pristine glass are present simultaneously.

Si-K edge and 710 eV for Fe-L edge) and another one before the edge (1840 eV for Si, 690 eV for Fe). Subtraction of images indicates the presence of silicon in the ICP and of iron in the GAL at nanometer scale.

Fe-L edge spectra were extracted from different zones of the GAL and ICP by collecting stacks at selected regions (Figure 7). Comparison with reference spectra of a Fe(II) iron carbonate (siderite – $FeCO_3$) and a Fe(III) oxyde (maghemite γ-Fe_2O_3), suggests that iron phases in the sample, both in ICP and in GAL, were mainly composed of Fe(III) species at nanometer scale.

Following the same data treatment as for Fe, spectra at the Si-K edge were extracted from ICP, GAL and the pristine glass SON 68. To compare to these spectra, STXM data were collected at Si-K edge on several references in the phyllosilicate family which can be formed in temperature and pressure conditions representative of the repository: a trioctahedral chlorite (chamosite), a trioctahedral serpentine (greenalite) and a dioctahedral smectite (nontronite) (Figure 8). All these phases present a same intense peak (noted A on Figure 8) at 1846 eV due to Si fourfold coordinated by O [13] and a peak at around 1855 eV (1855.2 eV for chamosite, 1855.1 eV for greenalite, 1855.9 eV for nontronite) (noted C on Figure 8). The authors associated peak C to a structured silicate. However the shape of peak B at 1850 eV varies depending on the type of iron-silicate, being absent in nontronite, but present as a shoulder in chamosite (1850.0 eV) and as a sharper peak in greenalite (1850.4 eV). Intensities of the broad band D at 1863 eV (1861.7 eV for chamosite, 1861.7 eV for greenalite, 1862.0 eV for nontronite), due to the contribution of neighbouring O, also slightly differ, depending on the phases (Figure 8).

Spectrum at Si-K edge obtained in the pristine glass in the sample has a single peak at 1846 eV. Absence of other peaks is linked to the absence of structure in the glass. On the contrary, spectra obtained in GAL and ICP presented a structured shape. Moreover they are quite similar to representative peaks at 1846 eV, 1855 eV (1856.2 for GAL, 1855.9 for ICP), and 1862 eV (Figure 9). The small shoulder at 1850.1 eV, present on the spectra of greenalite and chamosite but not on the one of nontronite is observable on the GAL and ICP spectra as well. Thus, this first comparison between references and sample spectra allows us to exclude the presence of pure nontronite but not to discriminate between chamosite and greenalite, or a mix of the three phases. Consequently, linear regression fits were performed with references (nontronite, chamosite, greenalite, pristine glass as an unstructured phase) and experimental spectra (GAL and ICP). Best fits are summarised in Table 3. Each time, a trioctahedral phyllosilicate was the main contribution (chamosite for type 1 fit, greenalite for type 2 fit). The total thickness of the simulated spectra (1 ± 0.1 µm), is in good agreement with the 'real' thickness of the thin foil, guaranteeing a reliable fit. These fitted spectra, are superimposed to experimental spectra on Figure 9.

Regarding the GAL, the fit including chamosite, showing a chi^2 of 0.00611 (type 1 fit) seems to be better than the one excluding this phase, 0.0163 (type 2 fit). This latter show a chi^2 2.7 times higher. Thus the main contribution for the experimental spectrum in GAL seems to be chamosite, with 71% total thickness equivalence. Moreover the shoulder on the experimental spectra (Figure 9(b)) at 1850.1 eV is better fitted using chamosite.

However concerning ICP the difference is very small between fits including chamosite and the one excluding it,

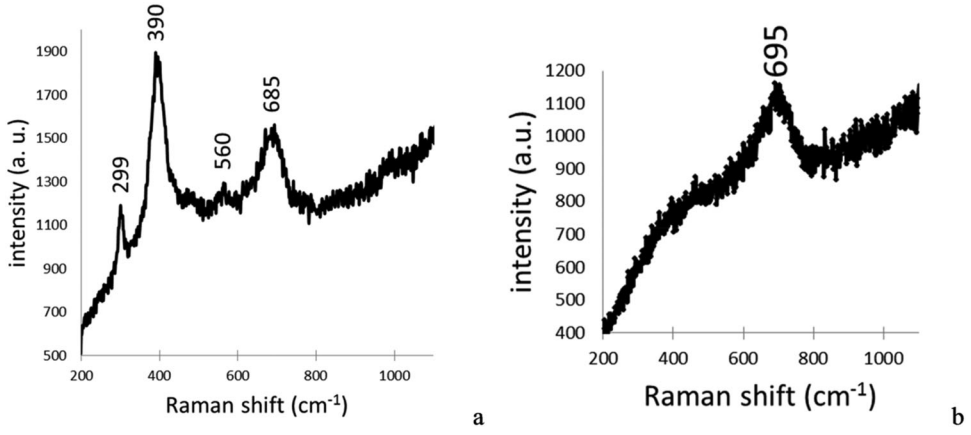

Figure 4. µRaman spectra obtained of iron corrosion products (ICP) of the canister. ICP are assimilated to goethite (in a) and ferrihydrite (in b), phases formed with iron(III).

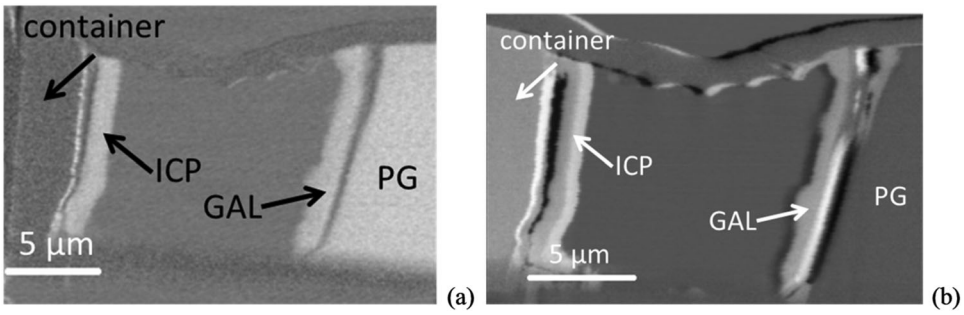

Figure 6. Spectral maps obtained with STXM on the FIB foil. (a) At Si-K edge, in white, presence of Si in iron corrosion products (ICP), in the glass alteration layer (GAL) and pristine glass (PG). (b) At Fe-L edge. Subtraction of two energies was chosen one at the edge (1846 eV for Si-K edge and 710 eV for Fe-L edge) and another one before edge (1840 eV for Si, 690 eV for Fe).

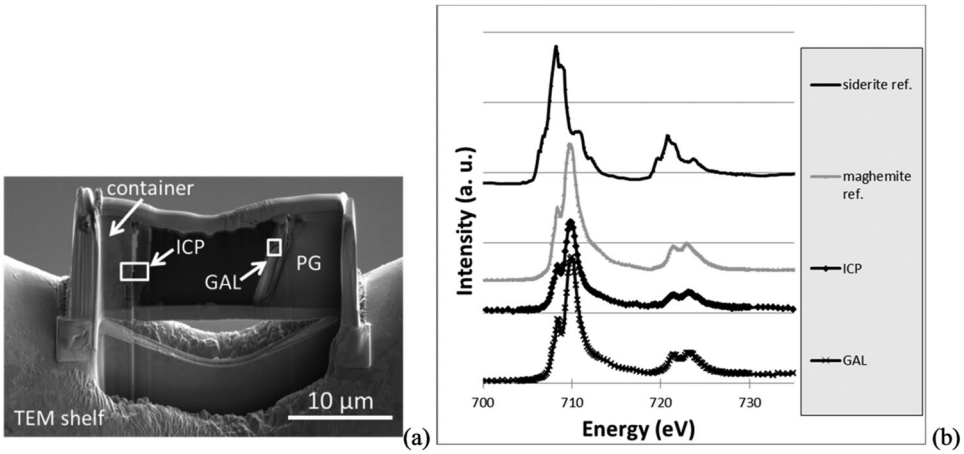

Figure 7. (a) Location of STXM analysis and (b) Fe-L edge spectra obtained in the iron corrosion products (ICP) and in the glass alteration layer GAL. Superposition with references of iron II (siderite Fe_2CO_3) and iron III (maghemite γ-Fe_2O_3) indicates three valent iron in the sample.

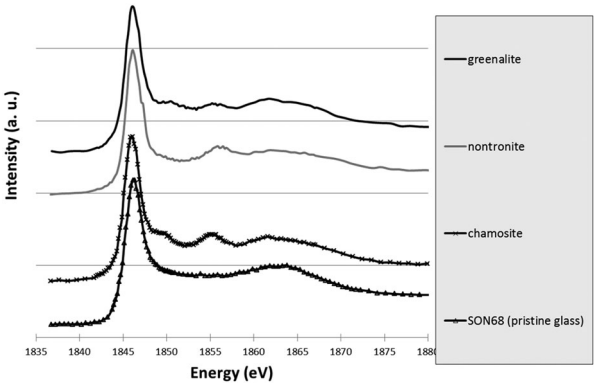

Figure 8. STXM Si-K edge reference spectra of greenalite (serpentine family), nontronite (smectite family), chamosite (chlorite family) and pristine glass.

with very close chi^2. It is not possible to discriminate between experimental spectrum and these reference spectra (Table 5).

Discussion

The microcontainer composed of nuclear glass and carbon steel surrounded by claystone and altered with water for 734 days in Andra's URL was analysed at different scales. All glass particles were observed to have GAL of 1 µm thick. SEM–EDS analysis at the micrometer scale showed that a GAL on the pristine glass was depleted in Na, Al, Ca and Zr and enriched in Fe. It was estimated that the dissolution rate in the GAL was 3.10^{-3} g m^{-2} d^{-1} assuming a constant dissolution rate. This dissolution rate is lower than the initial dissolution rate of SON68 glass in CO*x* water, 1.710^{-2} g m^{-2} d^{-1} at 50°C [14] and higher than the virtual residual rate in pure water (1.710^{-4} g m^{-2} d^{-1} at 90°C, [10]). Constant thickness of GAL suggests that the water is present everywhere in the container and that the distance from the source of the iron does not influence the dissolution kinetics of the PG. The loss of alkaline element (Na) demonstrates that hydration phenomenon took place. Concentration in Zr in GAL has drastically decreased, highlighting glass hydrolysis phenomenon. High concentration of iron, about 30%wt in the GAL, suggests that this element comes from the corrosion of the container.

Iron corrosion products on the internal face of the container have a high concentration of silicon, up to 20%wt. Traces of Mg, Al, Na and Ca have also been detected. Micro-Raman spectroscopy assimilates corrosion products as goethite (α-FeOOH) and a poor crystallised phase ferrihydrite (FeOOH.*n*H_2O) which is in agreement with the STXM results, indicating the presence of Fe(III) species. Anoxic and reducing conditions imposed by the environment foreshadowed ICP formed with Fe(II), and not Fe (III) [15]. The absence of these Fe(II) containing phases could be explained by the fact that corrosion products have evolved probably in contact with air between the dismantling of the sample and storage, despite all precautions.

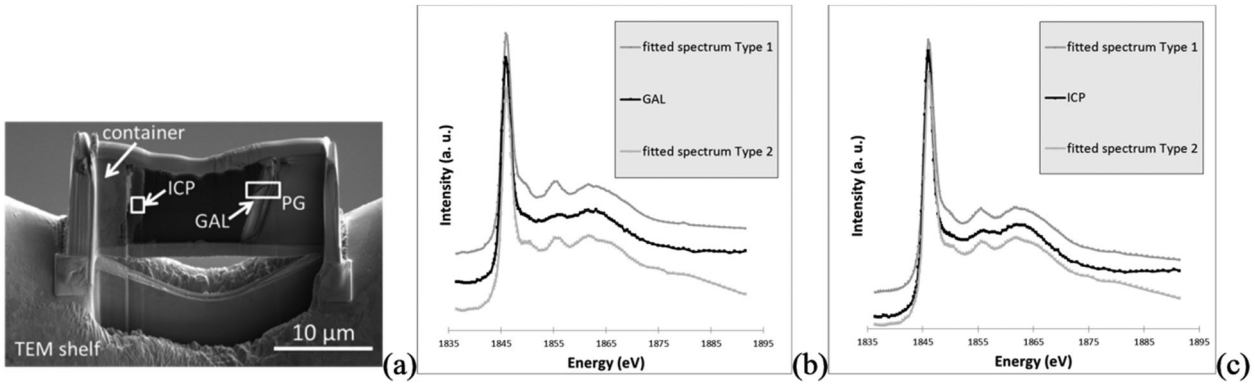

Figure 9. Location of STXM analysis (a). Experimental spectra and fitted spectra at Si-K edge obtained in the glass alteration layer (b) and in the iron corrosion products (c). Evidence of good correlation is shown between experimental spectra and fitted spectra.

Enrichment of Si in ICP and Fe in GAL has been investigated at the nanometer scale. Indeed neoformed phases in these areas may be responsible for this phenomenon. STXM results at Si-K edge have been acquired in ICP and in GAL, and compared to iron-silicate reference phases belonging to three different structural families (trioctahedral chlorite, trioctahedral serpentine and dioctahedral smectite). Contrary to the spectra obtained in the pristine glass, the ones collected in GAL presents a structure suggesting the presence of crystallised phases. STXM investigations, after comparison with the spectra obtained on the different reference phases, the closest is the one of Fe-rich trioctahedral chlorite family, the chamosite. However structural information given X-ray absorption spectra at Si-K edge considers other parameters than stack of sheets, such as the location of iron (in tetrahedrons and/or in octahedrons), tetrahedral or octahedral layer, Tschermak substitution etc. These data come from distances up to about 10 Å from the probed atom ([16], these Solenn). Consequently, other trioctahedral chlorites than chamosite, not tested here, could have very similar spectra. Thus, in the following, one will only discuss the presence of the trioctahedral chlorites family and not the specific one of chamosite. Usually authors define higher temperature and pressure than the ones of the present experiment for hydrothermal chlorite formation and stability [17]: a minima around 200°C and 1 kbar, while the alteration conditions for the sample does not exceed 50°C and 40 bars here. However, other authors report that conditions of formation for diagenetic chlorites are closer to the ones of the experiment described here [18–24]. Moreover Fe-rich chlorites formation needs precursor mineral such as saponite (trioctaedral smectite, reaction (1)), berthierine (trioctahedral serpentine, or kaolinite (reaction 2). Temperature of the transition between berthierine and chlorite (i.e. berthierine chloritisation) is still debated but is lower than for saponite chloritisation: berthierine chloritisation for Fe-rich trioctahedral chlorite (chamosite) could occur from 40°C for Texas Gulf coast chlorite and 80°C for Niger chlorite which crystallised in the lowest temperature conditions [25,26].

$$\begin{aligned} &Ca_{0.1}Na_{0.2}Fe_{1.1}MgAlSi_{3.6}O_{10}(OH)_2(\text{saponite}) \\ &+ 1.5Fe^{2+} + 1.2Mg^{2+} + 1.4Al^{3+} + 8.6H_2O \\ &\rightarrow Fe_{2.6}Mg_{2.2}Al_{2.4}Si_{2.8}O_{10}(OH)_8(\text{chlorite}) + 0.1Ca^{2+} \\ &+ 0.2Na^{2+} + 0.8SiO_2(\text{quartz}) + 9.2H^+ \end{aligned} \quad (1)$$

$$3Al_2Si_2O_5(OH)_4(\text{kaolinite}) + 9FeCO_3(\text{siderite}) + 2H_2O \rightarrow Fe_{9.0}Al_{6.0}Si_{6.0}O_{20}(OH)_{16}(\text{chlorite}) + SiO_2(\text{quartz}) + 9CO_2 \quad (2)$$

Solid-state transformation is the proposed mechanism to transform berthierine or saponite to chlorite under action of aqueous fluid [27,20,24]. Thus in the GAL, Fe-rich chlorite could be the product of chloritisation considering pressure and temperature conditions.

High silicon sorption capacity on corrosion products at neutral pH has been observed by several studies [28] and can explain high concentration of Si in the ICP. Silicon may come from glass alteration (under matrix hydrolysis) or from CO*x* water. Si-K edge absorption spectrum obtained in ICP differs from the amorphous one and was also structured. It seems to correspond to mix of several phases (nontronite, greenalite, chamosite, or others silicate phases), although best fits were obtained with trioctahedral phyllosilicates. Indeed nontronite has already been detected as the only Fe-silicate in ICP in the case of glass/iron alteration [3]. According to the same authors crystallised greenalite have been found in the GAL. Other authors [15,29] detected nontronite as the second or third main contribution of linear combination in the corrosion product layer in contact with CO*x* clay. Another author [30] has observed crystallised trioctahedral smectites in the GAL.

Table 5. Parameters of linear regressions performed with three or four reference spectra (nontronite + greenalite + glass SON68 and/or without chamosite) to fit experimental spectra in glass alteration layer and in iron corrosion products.

	Area	Contribution for linear regression	Total thickness	Chi²	M correlation
Type 1 fit (chamosite + nontronite + greenalite + SON 68)	GAL	71% chamosite + 25.5% nontronite + 3% pristine glass + 0.5% greenalite	0.8 µm	0.00611	0.996
	ICP	47% chamosite + 40.5% nontronite + 8.5% pristine glass + 4% greenalite	0.9 µm	0.025	0.993
Type 2 fit(nontronite + greenalite + SON 68)	GAL	62% greenalite + 37% nontronite + 1% pristine glass	0.7 µm	0.0163	0.99
	ICP	50% greenalite + 48% nontronite + 2% pristine glass	0.87 µm	0.0312	0.992

Conclusion and prospect

Products of alteration on glass/iron systems from the Andra's URL were identified and characterised through macro–micro–nanoscale investigations in order to understand the increase of glass alteration rate when it occurs near an iron source. An iron-rich phase, close to a trioctahedral chlorite, was identified in a glass alteration layer which could be formed from a serpentine precursor, according to temperature and pressure of the experiment in the Andra's URL. This result was obtained through a comparative approach between reference phyllosilicates and experimental samples, with scanning transmission X-ray microscopy technique at nanometer scale. Same technique performed in iron corrosion products did not allow the same identification, but suggest a complex mix of Fe-Si phases. At this stage a crucial step of the study is to increase the silicates reference database. It could enable to understand structural information contained in XANES spectrum at Si-K edge. In a complementary way, other methods will be implemented in the next future as, for example, TEM (including electron diffraction and HR observations).

To go further, the crystallinity of silicates present in the sample has to be studied, as well as the nature of iron corrosion products which can influence the family of neoformed silicates. Moreover, it is important to focus on the effect of the presence of iron-silicates on the protective behavior of the GAL. Further studies must also be conducted to better understand the way of formation of the GAL containing iron-silicates: dissolution and re-precipitation or glass hydrolysis.

Disclosure statement

No potential conflict of interest was reported by the authors.

ORCID

Charly Carriere http://orcid.org/0000-0002-1796-7539
Eddy Foy http://orcid.org/0000-0002-1381-2767
Nicolas Michau http://orcid.org/0000-0001-8387-4093

References

[1] ANDRA. Dossier 2005 Argile: synthesis – evaluation of the feasibility of a geological repository in an argillaceous formation, collection les rapports. Chatenay- Malabry, France, ANDRA (agence nationale pour la gestion des déchets radioactifs) 2005; 239.
[2] Grambow B. Nuclear waste glasses – how durable? Elements. 2006;2:357–364.
[3] Dillmann P, Gin S, Neff D, et al. Effect of natural and synthetic iron corrosion products on silicate glass alteration processes. Geochim Cosmochim Acta. 2016;172:287–305.
[4] Fournier M, Gin S, Frugier P. Resumption of nuclear glass alteration: state of the art. J Nucl Mater. 2014;448(1–3):348–363.
[5] Necib S, Linard Y, Martin C, et al. Iron/clay/glass interaction in compacted clay at 50°C, 2015, poster.
[6] Vinsot A, Mettler S, Wechner S. In situ characterization of the callovo-oxfordian pore water composition. Phys Chem Earth. 2008;33(Suppl 1):S75–S86.
[7] Dynes JJ, yliszczak T, Araki T, et al. Speciation and quantitative mapping of metal species in microbial biofilms using scanning transmission X-ray microscopy. Environ Sci Technol. 2006;40 (5):1556–1565.
[8] Rivard C, Montargès-Pelletier E, Vantelon D, et al. Combination of multi-scale and multi-edge X-ray spectroscopy for investigating the products obtained from the interaction between kaolinite and metallic iron in anoxic conditions at 90 °C. Phys Chem Miner. 2013;40(2):115–132.
[9] Manceau A, Drits VA, Lanson B, et al. Oxidation-reduction mechanism of iron in dioctahedral smectites: II. Crystal chemistry of reduced Garfield nontronite. Am Miner. 2000;85:153.
[10] Frugier P, Gin S, Minet Y, et al. SON68 nuclear glass dissolution kinetics: current state of knowledge and basis of the new GRAAL model. J Nucl Mater. 2008;380(1–3):8–21.
[11] Hanesch M. Raman spectroscopy of iron oxides and (oxy)hydroxides at low laser power and possible applications in environmental magnetic studies. Geophys J Int. 2009;177(3):941–948.
[12] Neff D, Bellot-Gurlet L, Dillmann P, et al. Raman imaging of ancient rust scales on archaeological iron artefacts for long-term atmospheric corrosion mechanisms study. J. Raman Spectrosc. 2006;37:1228–1237.
[13] Li D, Bancroft GM, Fleet ME, et al. Silicon K-edge XANES spectra of silicate minerals. Phys Chem Miner. 1995;22(2):115–122.
[14] Jollivet P, Gin S, Schumacher S. Forward dissolution rate of silicate glasses of nuclear interest in clay-equilibrated groundwater. Chem Geol. 2012;330–331:207–217.
[15] Schlegel ML, Bataillon C, Benhamida K, et al. Metal corrosion and argillite transformation at the water-saturated, high-temperature iron–clay interface: a microscopic-scale study. Appl Geochem. 2008;23(9):2619–2633.
[16] Levelut C, Cabaret D, Benoit M, et al. Multiple scattering calculations of the XANES Si-K edge in amorphous silica. J Non-Cryst Solids. 2001;293–295:100–104.
[17] Vidal O, Dubacq B. Thermodynamic modelling of clay dehydration, stability and compositional evolution with temperature, pressure and H_2O activity. Geochim Cosmochim Acta. 2009;73 (21):6544–6564.
[18] Velde B, Medhioub M. Approach to chemical equilibrium in diagenetic chlorites. Contrib Mineral Petrol. 1988;98(1):122–127.
[19] Hillier S, Velde B. Chlorite interstratified with a 7 mineral: an example from offshore Norway and possible implications for the interpretation of the composition of diagenetic chlorites. Clay Miner. 1992;27:475–486.
[20] Xu H, Veblen DR. Interstratification and other reaction microstructures in the chlorite-berthierine series. Contrib Miner Petrol. 1996;124(3):291–301.
[21] Aagaard P, Jahren JS, Harstad AO, et al. Formation of grain-coating chlorite in sandstones. laboratory synthesized vs. natural occurrences. Clay Miner. 2000;35(1):261–261.
[22] Worden RH, Morad S. Clay mineral cements in sandstones Richard H. Worden and Sadoon Morad. Special publication number 34 of the international association of sedimentologists; 2003; 489 p. Clays Clay Miner. 2004;52(1):139–140.
[23] Rigault C. Cristallochimie du fer dans les chlorites de basse temperature: implications pour la geothermometrie et la determination des paleoconditions redox dans les gisements d'uranium. France: University of Poitiers; 2010; 280.
[24] Beaufort D, Rigault C, Billon S, et al. Chlorite and chloritization processes through mixed-layer mineral series in low-temperature geological systems; a review. Clay Miner. 2015;50(4):497–523.
[25] Hillier S, Velde B. Octahedral occupancy and chemical composition of diagenetic (low-temperature) chlorites. Clay Miner. 1991;26(2):149–168.
[26] Inoue A, Meunier A, Patrier-Mas P, et al. Application of chemical geothermometry to low-temperature trioctahedral chlorites. Clays Clay Miner. 2009;57(3):371–382.
[27] Banfield Jillian F, Bailey Sturges W. Formation of regularly interstratified serpentine-chlorite minerals by tetrahedral inversion in long-period serpentine poly types. Am Miner. 1996;81:79.
[28] Philippini V, Naveau A, Catalette H, et al. Sorption of silicon on magnetite and other corrosion products of iron. J Nucl Mater. 2006;348(1–2):60–69.
[29] De Combarieu G, Schlegel ML, Neff D, et al. Glass–iron–clay interactions in a radioactive waste geological disposal: an integrated laboratory-scale experiment. Appl Geochem. 2011;26(1):65–79.
[30] Aréna H, Godon N, Rébiscoul D, et al. Impact of Zn, Mg, Ni and Co elements on glass alteration: additive effects. J Nucl Mater. 2016;470:55–67.
[31] Reguer, S. Phases chlorées sur les objects archéologiques ferreux corrodés dans les sols: caractérisations et mécanismes de formation [thesis]. Orsay: University Paris XI; 2005.